On-Chip Laser-Driven Free-Electron Spin Polarizer

Clarisse Woodahl,[*] Melanie Murillo, Charles Roques-Carmes, Aviv Karnieli,
David A. B. Miller, and Olav Solgaard
E. L. Ginzton Laboratory, Stanford University, Stanford, California 94305, USA

(Received 23 July 2025; accepted 9 January 2026; published 12 February 2026)

Spin-polarized electron beam sources enable studies of spin-dependent electric and magnetic effects at the nanoscale. We propose a method of creating spin-polarized electrons on an integrated photonics chip by laser-driven nanophotonic fields. A two-stage interaction separated by a free-space drift length is proposed, where the first stage and drift length introduces spin-dependent characteristics into the probability distribution of the electron wave function. The second stage uses an adjusted optical near field to rotate the spin states utilizing the spin-dependent wave-packet distribution to produce electrons with high ensemble average spin expectation values. This platform provides an integrated and compact method to generate spin-polarized electrons, implementable with millimeter scale chips and tabletop lasers.

DOI: 10.1103/3c1m-d3hh

Introduction—The Stern-Gerlach (SG) experiment revealed the quantized nature of electron spins within neutral atoms utilizing spin-dependent magnetic-field gradient forces [1]. The same apparatus to create spin-polarized free electrons cannot be implemented due to particle momentum-position uncertainty and Lorentz force blurring [2]. Spin-polarized electron beams, which have become an indispensable tool for probing fundamental characteristics of matter [3–7], have been produced through methods that include spin-polarized photocathodes using semiconductors [4,8,9], self-polarizing interactions of relativistic electrons in storage rings (the Sokolov-Ternov effect [10,11]), and proposed in high intensity free-space interactions like the Kapitza-Dirac effect [12–14], or Compton scattering [15]. These methods introduce challenges limiting their accessibility, including cathode maintenance for spin-polarized sources, and high laser intensities for free-space interactions.

These challenges have promoted the continued exploration of methods to produce spin-polarized electrons. Work by Pan and Xu [16] suggested the use of optical near fields to generate such beams. This method is attractive due to the reduced laser intensities required and the potential to achieve large beam polarization. Structure-mediated near-field-electron interactions have been demonstrated in dielectric laser accelerators [17–21], making similar geometries to implement spin-dependent interactions experimentally feasible.

Here, we propose a two-stage approach using magnetic near fields to produce spin-polarized electrons. We show an on-axis SG-type setup for free electrons to break spin-state symmetry [22,23]. We exploit intense magnetic-field gradients created by rapid field oscillations of periodic grating near fields, to impart efficient spin-dependent longitudinal forces parallel to the electron propagation axis [16,22,23]. The second interaction stage polarizes electrons toward the same transverse spin state. We show 70% beam polarization, defined as the normalized difference between the number of electrons measured in one spin eigenstate and the other, can be achieved in the proposed devices without loss of beam brightness or the need for external bending magnets. The proposed 70% polarization produced on chip from an unpolarized source is above the theoretical maximum of a standard GaAs semiconductor source and comparable to strained GaAs-GaAsP lattices. [24].

Spin polarizer operating principles—The proposed spin-polarizing structure is shown in Fig. 1, consisting of two stages of dual-pillar gratings separated by a drift length, L_D, where each pair of dual pillars along the gratings is separated by a channel width on the order of a few tens to hundreds of nanometers to allow electrons to propagate through the structure from left to right. Both dual-pillar grating stages are illuminated on each side with counter-propagating transverse electric (TE) plane waves, where the magnetic field is polarized along the electron propagation axis, the z axis, to mitigate electric field scattering. The illuminated subwavelength gratings produce channel modes that can be decomposed into near-field spatial harmonics [25]. Phase matching for synchronous propagation of the first harmonic and electrons traveling through the channel center can be performed by tuning the laser

---

[*] Contact author: cwoodahl@stanford.com

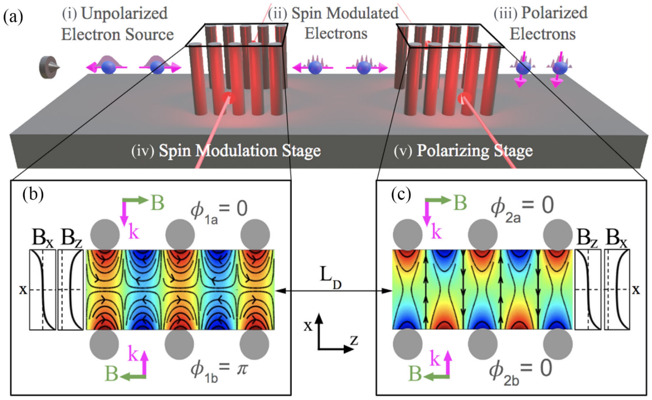

FIG. 1. Mechanism for generation of spin-polarized electron beams on a chip. (a) Schematic of the proposed two-stage interaction set-up. The first stage and following free-space propagation introduces spin-dependent density formations and the second stage rotates the spin states to produce a polarized beam. (b),(c) First harmonic magnetic field profiles of modulation and polarizing stages, respectively. Corresponding cosh and sinh transverse profiles of B_x and B_z, and relative phases for defined illuminants are shown.

wavelength and grating periodicity to fulfill $\lambda_g = \beta\lambda$, where $\beta = v_{el}/c$ is the electron's relativistic fraction, λ is the free-space laser wavelength, and λ_g is the grating period. The first-harmonic near field oscillates sinusoidally along the electron propagation axis with the wave vector $k_z = 2\pi/\lambda_g$. A subrelativistic electron phase-matched to near-infrared laser wavelengths has a λ_g on the order of a few hundred nanometers, leading to rapid spatial oscillation of the near field and a large amplitude magnetic-field gradient force for spin-dependent interactions.

When the dual-pillar gratings are driven by counter-propagating plane waves, the evanescent near fields interfere based on the relative phases between the plane waves. Figure 1(b) has the relative phases between the plane waves set so the longitudinal magnetic fields interfere constructively in the channel center, therefore creating what we denote as the first-harmonic cosh mode for longitudinal spin separation. The cosh mode exhibits cosh B_z profile and a sinh B_x profile along $\hat{x}$. Figure 1(c) has the relative phases between the plane waves set so the longitudinal magnetic field interferes destructively in the channel center, therefore creating our denoted first-harmonic sinh mode used for spin rotations. The sinh mode has a sinh B_z profile and cosh B_x profile along $\hat{x}$.

Sinusoidal forces, created by near-field harmonics acting on free electron wave packets, have been previously shown to impart spin-independent energy modulation leading to density bunch formations within the wave packet after a free-space drift length using transverse-magnetic (TM) photon-induced near-field microscopy (PINEM) [26,27]. When the illumination is rotated from TM to TE, as in our proposed device, magnetic-field interactions can dominate, leading to a spin-dependent sinusoidal force acting on the free electron wave packet. In the next section we will formulate expressions for spin-dependent wave-packet modulations occurring in the proposed TE illuminated structure.

Theory—TE spin-density bunch formation: To predict the spin-dependent bunching behavior of free electrons with unpolarized spins defined along the axis of propagation, $\hat{z}$, we consider a TE dual-drive field with the $\vec{E}$ field polarized along infinitely tall pillars [see Fig. 1(a)]. The dual-drive fields will be π phase-shifted, creating a cosh B_z mode as shown in Fig. 1(b) [25,28].

We consider an electron wave packet transversely defocused along the direction of the pillars, such that we can assume it is effectively diffractionless along this direction [see more details in Supplemental Material (SM) [28] Sec. V]. The complex dimensionless magnetic coupling coefficient can be defined as

$$g_B = \frac{-i\mu_B k_z}{\hbar\omega} \int_{-L/2}^{L/2} B_z(z) e^{-ik_z z} dz, \tag{1}$$

where μ_B is the Bohr magneton, $B_z(z)$ is the complex longitudinal magnetic field amplitude in the channel center, and ω is the laser angular frequency. With this definition we can perform time evolution on an initial electron wave packet using the Pauli interaction Hamiltonian [31]

$$\hat{\mathcal{H}}_I = \frac{e}{m_e c}\mathbf{A}(\mathbf{r},t)\cdot\hat{\mathbf{p}} + \mu_b \mathbf{B}(\mathbf{r},t)\cdot\vec{\sigma} + \frac{e^2}{2m_e c^2}\mathbf{A}^2(\mathbf{r},t), \tag{2}$$

where $\mathbf{A}(\mathbf{r},t)$ is the vector potential field, $\hat{\mathbf{p}}$ is the momentum operator, m_e is the free electron mass, e is the electron charge, and $\vec{\sigma} = [\sigma_x, \sigma_y, \sigma_z]$ are the Pauli matrices. Unlike conventional PINEM with TM modes (where the electric field is aligned with the electron velocity), which is dominated by the $A \cdot p$ term in the Hamiltonian, here the coupling to the TE mode dominates through the $B \cdot \sigma$ term. Applying the time evolution operator defined from the interaction Hamiltonian and the Jacobi-Anger expansion, the wave function after the interaction is found. Following free-space drift, the quadratic photon-order-dependent accumulated phase can be included [32] to obtain the density-modulated wave function,

$$\psi'_{\pm}(z') = \psi^0_{\pm}(z') \sum_n \mathcal{J}_n(2|g_{B_1}|) \exp\left(ink_z z' + in\phi_1\right) \times \exp\left(in\left(-\frac{\pi}{2} \pm \frac{\pi}{2}\right) - in^2\pi\frac{L_D}{L_{QR}}\right), \tag{3}$$

where $\psi^0_{\pm}(z')$ are the initial spin-dependent electron wave functions in space, $\mathcal{J}_n$ is the n th order Bessel function of the first kind, g_{B_1} is the magnetic coupling coefficient defined in Eq. (1), z' is the position offset from the packet center z_o, ϕ_1, the interaction phase, is the argument of g_{B_1}, L_D is the free-space drift length, and $L_{QR} \approx \beta^3 m_e c\lambda^2/h$, is the quantum

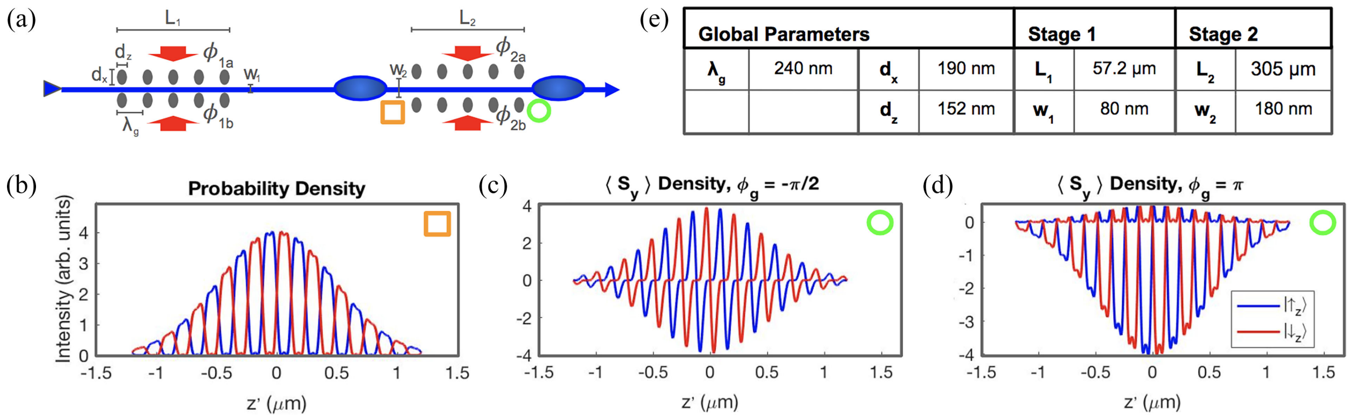

Global Parameters				**Stage 1**		**Stage 2**	
λ_g	240 nm	d_x	190 nm	L_1	57.2 μm	L_2	305 μm
		d_z	152 nm	w_1	80 nm	w_2	180 nm

FIG. 2. Spin-dependent electron densities. (a) Experimental schematic. The positions where the electron density or spin density is calculated are highlighted by an orange square and a green circle. (b) Spin-dependent electron probability density distribution after interaction with first stage and free-space drift; input spin states differentiated by color. (c),(d) Electron y-axis spin density immediately following interaction with the second stage: (c) has a relative interaction phase between stage 1 and 2 of $-\pi/2$, leading to $\langle S_y\rangle \approx 0$; (d) has a relative interaction phase between stage 1 and 2 of π, which results in $\langle S_y\rangle \approx -0.7\hbar/2$. (e) Summary of example pillar geometry values as denoted in (a).

revival length defined in [32]. The quantum revival length describes the free-space drift length an electron travels to observe density distribution revivals due to free electron dispersion. This result assumes a small initial longitudinal momentum spread and negligible longitudinal dispersion over interactions lengths.

The $\pm$ subscript corresponds to electrons initially polarized in the spin-up or spin-down state along $\hat{z}$. The spin states are defined as $|\uparrow\rangle = [\cos(\theta/2), \sin(\theta/2)e^{i\phi}]^T$ and $|\downarrow\rangle = [\sin(\theta/2), -\cos(\theta/2)e^{i\phi}]^T$, with polar coordinates $\theta = 0$ and $\phi = \pi$ used for the $\hat{z}$ spin quantization axis. The photon-order-dependent phase factors exhibit an additional π phase shift for odd photon-order interactions on $|\downarrow_z\rangle$ electrons due to the sign flip $\sigma_z|\downarrow_z\rangle = -|\downarrow_z\rangle$. The additional π phase for the spin-down electrons leads to a spatial π phase shift in density bunch formation, as seen in Fig. 2(b). The probability distribution initially of $|\uparrow_z\rangle$ and $|\downarrow_z\rangle$ electron states is significantly separated into separate time bins following the first interaction stage and free-space drift. There is minimal overlap between the up-spin and down-spin states' probability densities at $L_D = L_{QR}/2$, with small depolarizing contributions from the edges of the bunches. Minimizing the overlap enhances the degree of achievable spin polarization. The sinh B_x mode suppresses transverse magnetic-field spin contributions along the channel center [28].

One of the main implications of Eq. (3) and the resulting time bin separation of Fig. 2(b) is mapping the initial spin states $|\uparrow_z\rangle$ and $|\downarrow_z\rangle$, which initially share the same spatial wave packet ψ^0, into separate bins, constituting a general unitary transformation U_{SG} that entangles the spin degree of freedom with longitudinal position. Explicitly, we have $U_{\mathrm{SG}}|\uparrow_z, \psi^0\rangle = |\uparrow_z, \psi'_+\rangle$ and $U_{\mathrm{SG}}|\downarrow_z, \psi^0\rangle = |\downarrow_z, \psi'_-\rangle$, where $\psi'_\pm$ are close to being orthogonal. Importantly, this transformation holds true for initially mixed spin states $\rho_{\mathrm{spin}} \otimes |\psi^0\rangle\langle\psi^0|$ (see further analysis in SM Sec. VI). In the next section, we will demonstrate how the second interaction stage acts on the two wave packets $\psi'_\pm$ to rotate their respective spins to be aligned with the same direction, effectively polarizing the beam.

Creating high polarization electrons: In the previous section we detailed a method to create spin-dependent electron wave-packet distributions. These wave packets can be used to create high polarization electron spin distributions regardless of the initial spin state.

Achieving high polarization relies on the π spatial phase shift between spin-dependent wave packets, i.e., a $|\uparrow_z\rangle$ state's probability density is phase-matched around ϕ, while the $|\downarrow_z\rangle$ state's probability density is phase-matched around $\phi + \pi$. Given a wave packet resulting from the spin-dependent modulation interacting with a cosh-transverse magnetic-field mode [see Fig. 1(c)], the field will induce spin rotations. With properly chosen interaction strengths, coupled with the spin-dependent spatial π phase shifts in the probability density function, the expectation value of the final spin state can be polarized toward either the $|\uparrow_y\rangle$ state or the $|\downarrow_y\rangle$ state along the y axis.

The dominating final spin state is dependent on the injection timing of the spin-dependent wave packet into the second stage. This timing is defined by the difference between the first and second stage interaction phases of the wave-packet center, z_o, into the copropagating first-harmonic fields of each stage. Explicitly, the final spin state can be chosen by tuning $\phi_g = \phi_1 - \phi_2$.

A similar coupling strength can be defined for the transverse magnetic-field interaction of the second stage, by replacing $B_z(z)$ with $B_x(z)$ in Eq. (1). Following the second stage interaction, the state can be given by

$$|\psi''\rangle = \int dz' \sum_{s=\uparrow,\downarrow} \psi'_s(z') \sum_m \mathcal{J}_m(2|g_{B_2}|) \times \exp(imk_z z' + im\phi_2)\sigma_x^m |z', s_z\rangle, \tag{4}$$

where g_{B_2} and ϕ_2 are the interaction strength and phase of the second stage, and $|z', s_z\rangle = |z'\rangle \otimes |s_z\rangle$ denotes the position and spin bases with eigenvalues z' and $s_z \in \{\uparrow_z, \downarrow_z\}$ on which the wave function, $\psi'_s(z')$, as given in Eq. (3), is projected.

Expanding the wave function [Eq. (4)] into even-photon order, spin-preserving interactions, and odd-photon order, spin-rotating interactions, the spin-expectation value along the y axis can be described for an arbitrary initial spin state,

$$\langle \hat{S}_y \rangle = \frac{\hbar}{2} \int dz' (|c_+|^2 |\psi'_+(z')|^2 - |c_-|^2 |\psi'_-(z')|^2) \sin(2\alpha(z')) + 2|c_+||c_-| \cos(2\alpha(z')) \Re\left\{ i e^{i\phi_{d_\pm}} \psi'_+(z') \psi'^*_-(z') \right\}, \tag{5}$$

where c_+ and c_- are the coefficients for an arbitrary initial superposition state of $|\uparrow_z\rangle$ and $|\downarrow_z\rangle$, respectively, $\phi_{d_\pm} = \arg(c_+) - \arg(c_-)$ and $\alpha(z') = 2|g_{B_2}|\sin(k_z z' + \phi_2)$. The prefactor from Eq. (4) can be collapsed into the sine term in the spin-expectation value in Eq. (5). The outer sine term holds information about the cyclic nature of the spin rotation. As the interaction becomes stronger (equivalently, as the $|g_{B_2}|$ factor increases), additional spin-rotating oscillations are introduced from the spatially varying magnetic field. This spatially varying spin factor is then multiplied onto the probability density function to obtain a spin-weighted probability distribution. Equation (5) can also describe the polarization of mixed spin states with density matrix $\rho_{\kappa\kappa'}, \kappa, \kappa' = \pm$, by replacing $|c_\pm|^2$ with $\rho_{\pm\pm}$ and $c_\pm c^*_\mp$ with $\rho_{\pm\mp}$.

Figures 2(c) and 2(d) show the effect of tuning ϕ_g on the final spin distribution. Figure 2(c) shows an example where net spin polarization is not enhanced. Figure 2(d) shows an example where the spin polarization is enhanced and tuned toward a $|\downarrow_y\rangle$ state. The spin-weighted probability distribution shown in Fig. 2(d) equates to a spin expectation value of $\approx -0.7\hbar/2$, which corresponds to a beam polarization percentage of approximately 70%, or equivalently a probability of measuring a spin-down particle, $P_{\downarrow_y} \approx 85\%$ and spin-up, $P_{\uparrow_y} \approx 15\%$. Calculations were performed considering initial spin states of $|\uparrow_z\rangle$ or $|\downarrow_z\rangle$, representing a maximally mixed input state $\rho = 1/2|\uparrow_z\rangle\langle\uparrow_z| + 1/2|\downarrow_z\rangle\langle\downarrow_z|$ when averaged. Thus, from the density matrix description and Eq. (5), various state mixtures resulting in a maximally mixed input beams can achieve ≈70% polarization with our considered electron beam and laser parameters. These parameters include low energy spread electrons with $\sigma_E = 0.15$ eV, subrelativistic initial electron energy with $\beta = 0.1$ to enable proper treatment by the Pauli Hamiltonian [16], laser wavelength of 2.4 μm, and corresponding $\lambda_g = 240$ nm. Additionally, the first interaction region electric field strength E_y and interaction length L is tuned so that only a couple orders of photon absorptions and emissions lead to significant contributions in the wave structure of the electron, or $|g_{B_1}| \approx 0.5$. After the spin-dependent modulation of the first stage, a drift length $L_{QR}/2$ is chosen for maximal contrast [32]. The second interaction length and field strength is tuned so $|g_{B_2}| \approx 0.5$, to maximize the first-order photon exchange and minimize higher order exchanges.

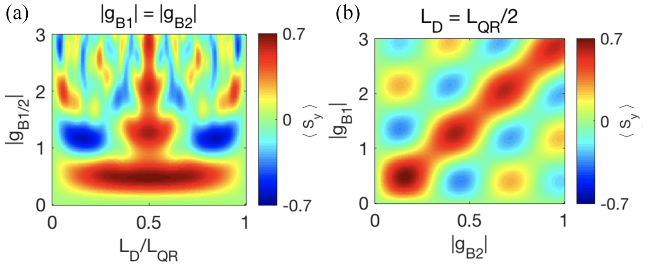

FIG. 3. Influence of experimental parameters. (a) Heat map of $\langle S_y \rangle$ in terms of the drift length and coupling strength parameters, with the condition $|g_{B1}| = |g_{B2}|$. Notably, high polarization shows minimized drift length dependence for $|g_{B_1}| = |g_{B_2}| \approx 0.5$, corresponding to microbunches with significant temporal coherence. (b) Heat map of $\langle S_y \rangle$ in terms of $|g_{B1}|$ and $|g_{B2}|$, depicting higher order overlaps when the drift length is half the quantum revival length.

The discussed set of conditions give a large overlap between portions of high z-axis spin density and spin-rotating magnetic fields, enabling the creation of highly polarized electrons. Figure 3 maps the value of $\langle \hat{S}_y \rangle$ when $\phi_g = 0$ in two cases. Figure 3(a) maps varying $|g_{B_{1/2}}|$ and L_D/L_{QR}, when $|g_{B_1}| = |g_{B_2}| = |g_{B_{1/2}}|$. High spin-polarization effects are observed over a significant range of L_D values for moderate magnetic coupling coefficients, while increased magnetic coupling factors see a reduction in spin-polarization magnitude and acceptable drift range. Moderate $|g_B|$ factors benefit coherence lengths for density bunches and minimize quadratic phase accumulation within interaction regions. The sub-wave-packet spin separation inherent to the proposed interaction enables the use of longitudinally extended electrons, further improving coherence lengths. Figure 3(b) depicts the one-to-one linear relationship between the coupling factor in the first and second stage when L_D is half L_{QR}. The moderate and equal coupling coefficients exhibit significant spin polarization and strong temporal coherence.

Experimental considerations—A commercial femtosecond laser can provide the needed fields for spin polarization on a chip. Considering the requirement of $|g_{B_{1/2}}| \approx 0.5$ and the electron beam parameters discussed above, we choose an interaction length of 52.7 μm for the first interaction stage, an achievable conversion efficiency from incident field strength to field strength in the channel center of 0.057, and incident complex electric field amplitude (half-peak) of 750 MV/m on each dual-drive side. An elliptical silicon pillar with x diameter of 190 nm and z diameter of 152 nm, and channel width of 80 nm were simulated using finite-difference time-domain simulations (Flexcompute Tidy3D) to achieve the desired 0.057 conversion efficiency. Figures 2(a) and 2(e) summarize the geometries of the simulated pillars. In the second stage a wider channel width of 180 nm, with a reduced conversion efficiency of 0.0106 and increased interaction length of ~305 μm, can be used to suppress ponderomotive interactions. In higher intensity regimes, the ponderomotive force can lead to momentum contributions and bunching that can retain a similar spin-polarizing degree [see SM [28] Sec. VII for a discussion of bunching dynamics during the interaction region]. Peak fields of 550 MV/m have been shown to be under the laser induced damage threshold of hydrogen-annealed processed silicon pillars for 300 fs, 1.96 μm laser pulses [33]. Longer wavelengths are expected to exhibit higher laser induced damage thresholds [34]. The use of a pulse front tilt has been demonstrated to improve interaction time [35,36], and could be used with shorter laser pulses to further increase peak fields.

Realistic electron beam parameters are important for experimental implementation. We note that, due to the only electric field contributions being E_y, the $\hat{p} \cdot \hat{A}$ term of the Pauli Hamiltonian that was neglected previously would be sensitive to v_y within the transverse electron wave packet. Additionally, for the first stage where PINEM interactions would degrade the fidelity of the spin-dependent microbunches, E_y exhibits a sinh mode along the x axis around the center of the channel, and thus vanishes at the position of the electron beam.

In the cases where the electron beam is highly collimated in the y direction and focused in the x direction throughout the interaction region, nonzero photon order terms can be heavily attenuated. An astigmatic beam with such characteristics can provide high fidelity spin distributions and naturally fits the geometry of a dielectric laser accelerator with a narrow x-axis channel, and very tall pillars in the y direction (see SM [28] Sec. V).

Conclusions—We have proposed a single-chip, two-stage device to produce a polarized electron beam from an initially unpolarized beam. Because it converts spin orthogonalities into time-based orthogonalities, the two-stage interaction is a powerful operation to polarize arbitrary unpolarized initial state mixtures. No external bending magnets are required for the creation of high polarization beams. Switching between final state polarization can be performed by tuning the relative phases of the two stages. Reducing the requirement of external magnetic fields opens the door for efficient on-axis integration with PINEM and other photonic on-chip technology, such as focusing structures or photonic guiding structures.

Beyond creation of significantly polarized electrons, near-field-based momentum modulations and spin rotations can create more complex spin superposition states and probability-density structures within the electron wave packet. The wave-packet formalism is of interest to free-electron quantum optics, an increasingly explored research area [37], where spin-dependent dynamics may add interesting additional degrees of freedom to carry and manipulate quantum information held by free electrons. The fine spin and momentum structure created within the electron wave packet could present TE and TM PINEM prepared electrons as unique probes for ultrafast experiments and imaging of spin-dependent properties.

Acknowledgments—C. W. and M. M. acknowledge support by the National Science Foundation Graduate Research Fellowship Program under Grant No. DGE-2146755. C. R.-C. is supported by a Stanford Science Fellowship. A. K. is supported by the VATAT-Quantum fellowship by the Israel Council for Higher Education, the Urbanek-Chodorow postdoctoral fellowship by the Department of Applied Physics at Stanford University, the Zuckerman STEM leadership postdoctoral program, and the Viterbi fellowship by the Technion.

Data availability—The data that support the findings of this article are openly available [38].

[1] W. Gerlach and O. Stern, Der experimentelle Nachweis der Richtungsquantelung im Magnetfeld, Z. Phys. **9**, 349 (1922).

[2] N. F. Mott, The scattering of fast electrons by atomic nuclei, Proc. R. Soc. A **124**, 425 (1929).

[3] M. Kuwahara, Y. Yoshida, W. Nagata, K. Nakakura, M. Furui, T. Ishida, K. Saitoh, T. Ujihara, and N. Tanaka, Intensity interference in a coherent spin-polarized electron beam, Phys. Rev. Lett. **126**, 125501 (2021).

[4] D. T. Pierce, R. J. Celotta, G. Wang, W. N. Unertl, A. Galejs, C. E. Kuyatt, and S. R. Mielczarek, The GaAs spin polarized electron source, Rev. Sci. Instrum. **51**, 478 (1980).

[5] D. T. Pierce, Spin-polarized electron microscopy, Phys. Scr. **38**, 291 (1988).

[6] M. Kuwahara, S. Kusunoki, Y. Nambo, K. Saitoh, X. Jin, T. Ujihara, H. Asano, Y. Takeda, and N. Tanaka, Coherence of a spin-polarized electron beam emitted from a semiconductor photocathode in a transmission electron microscope, Appl. Phys. Lett. **105**, 193101 (2014).

[7] M. L. Swartz, Physics with polarized electron beams, SLAC Pub **4656**, 22 (1988).

[8] D. T. Pierce, F. Meier, and P. Zürcher, Negative electron affinity GaAs: A new source of spin-polarized electrons, Appl. Phys. Lett. **26**, 670 (1975).

[9] D. T. Pierce and F. Meier, Photoemission of spin-polarized electrons from GaAs, Phys. Rev. B **13**, 5484 (1976).

[10] A. A. Sokolov and I. M. Ternov, On polarization and spin effects in the theory of synchrotron radiation, Sov. Phys. Dokl. **8**, 1203 (1964).

[11] A. A. Sokolov and I. M. Ternov, Synchrotron radiation, Russ. Phys. J. **10**, 39 (1967).

[12] S. Ahrens, H. Bauke, C. H. Keitel, and C. Müller, Spin dynamics in the Kapitza-Dirac effect, Phys. Rev. Lett. **109**, 043601 (2012).

[13] R. Erhard and H. Bauke, Spin effects in Kapitza-Dirac scattering at light with elliptical polarization, Phys. Rev. A **92**, 042123 (2015).

[14] Y. Wang and S. Ahrens, Parameter-space investigation for spin-dependent electron diffraction in the Kapitza-Dirac effect, Phys. Rev. A **109**, 012212 (2024).

[15] G. Bhatt, H. Grotch, E. Kazes, and D. A. Owen, Relativistic spin-dependent Compton scattering from electrons, Phys. Rev. A **28**, 2195 (1983).

[16] D. Pan and H. Xu, Polarizing free electrons in optical near fields, Phys. Rev. Lett. **130**, 186901 (2023).

[17] E. A. Peralta, K. Soong, R. J. England, Z. Wu, B. Montazeri, C. McGuinness, J. McNeur, K. J. Leedle, R. F. Pease, R. L. Byer *et al.*, Demonstration of electron acceleration in a laser-driven dielectric microstructure, Nature (London) **503**, 91 (2013).

[18] K. J. Leedle, R. Fabian Pease, R. L. Byer, and J. S. Harris, Laser acceleration and deflection of 96.3 keV electrons with a silicon dielectric structure, Optica **2**, 158 (2015).

[19] K. J. Leedle, D. S. Black, Y. Miao, K. E. Urbanek, A. Ceballos, H. Deng, J. S. Harris, O. Solgaard, and R. L. Byer, Phase-dependent laser acceleration of electrons with symmetrically driven silicon dual pillar gratings, Opt. Lett. **43**, 2181 (2018).

[20] K. P. Wootton, Z. Wu, B. M. Cowan, A. Hanuka, I. V. Makasyuk, E. A. Peralta, K. Soong, R. L. Byer, and R. J. England, Demonstration of acceleration of relativistic electrons at a dielectric microstructure using femtosecond laser pulses, Opt. Lett. **41**, 2696 (2016).

[21] J. Breuer and P. Hommelhoff, Laser-based acceleration of nonrelativistic electrons at a dielectric structure, Phys. Rev. Lett. **111**, 134803 (2013).

[22] H. Batelaan, T. J. Gay, and J. J. Schwendiman, Stern-Gerlach effect for electron beams, Phys. Rev. Lett. **79**, 4517 (1997).

[23] G. A. Gallup, H. Batelaan, and T. J. Gay, Quantum-mechanical analysis of a longitudinal Stern-Gerlach effect, Phys. Rev. Lett. **86**, 4508 (2001).

[24] J. Grames and M. Poelker, *Polarized Electron Sources* (Springer International Publishing, Cham, 2023), pp. 261–284, ISBN 978-3-031-16715-7.

[25] D. S. Black, Z. Zhao, K. J. Leedle, Y. Miao, R. L. Byer, S. Fan, and O. Solgaard, Operating modes of dual-grating dielectric laser accelerators, Phys. Rev. Accel. Beams **23**, 114001 (2020).

[26] B. Barwick, D. J. Flannigan, and A. H. Zewail, Photon-induced near-field electron microscopy, Nature (London) **462**, 902 (2009).

[27] S. T. Park, M. Lin, and A. H. Zewail, Photon-induced near-field electron microscopy (PINEM): theoretical and experimental, New J. Phys. **12**, 123028 (2010).

[28] See Supplemental Material at http://link.aps.org/supplemental/10.1103/3c1m-d3hh for detailed discussions and derivations, which includes Refs. [30,31].

[29] D. S. Black, U. Niedermayer, Y. Miao, Z. Zhao, O. Solgaard, R. L. Byer, and K. J. Leedle, Net acceleration and direct measurement of attosecond electron pulses in a silicon dielectric laser accelerator, Phys. Rev. Lett. **123**, 264802 (2019).

[30] B. Bransden and C. Joachain, Quantum Mechanics, *Quantum Mechanics*, 2nd ed. (Pearson Education, Harlow, England, 2000), ISBN 9780582356917.

[31] D. A. Miller, *Quantum Mechanics for Scientists and Engineers* (Cambridge University Press, New York, 2008), ISBN 9780521897839.

[32] M. V. Tsarev, A. Ryabov, and P. Baum, Free-electron quits and maximum-contrast attosecond pulses via temporal Talbot revivals, Phys. Rev. Res. **3**, 043033 (2021).

[33] Y. Miao, D. S. Black, K. J. Leedle, Z. Zhao, H. Deng, A. Ceballos, R. L. Byer, J. S. Harris, and O. Solgaard, Surface treatments of dielectric laser accelerators for increased laser-induced damage threshold, Opt. Lett. **45**, 391 (2020).

[34] K. Werner, V. Gruzdev, N. Talisa, K. Kafka, D. Austin, C. M. Liebig, and E. Chowdhury, Single-shot multi-stage damage ablation of silicon by femtosecond mid-infrared laser pulses, Sci. Rep. **9**, 19993 (2019).

[35] D. Cesar, J. Maxson, X. Shen, K. P. Wootton, S. Tan, R. J. England, and P. Musumeci, Enhanced energy gain in a dielectric laser accelerator using a titled pulse front laser, Opt. Express **26**, 29216 (2018).

[36] P. Broaddus, T. Egenolf, D. S. Black, M. Murillo, C. Woodahl, Y. Miao, U. Niedermayer, R. L. Byer, K. J. Leedle, and O. Solgaard, Subrelativistic alternating phase focusing dielectric laser accelerators, Phys. Rev. Lett. **132**, 085001 (2024).

[37] R. Ruimy, A. Karnieli, and I. Kaminer, Free-electron quantum optics, Nat. Phys. **21**, 193 (2025).

[38] C. Woodahl, “Free Electron Spin Polarizer”, 10.5281/zenodo.18225582 (2026).